

# High-Resolution Ultrasonic Imaging of Dento-Periodontal Tissues Using a Multi-Element Phased Array System

KIM-CUONG T. NGUYEN,<sup>1,2</sup> LAWRENCE H. LE,<sup>2,3</sup> NEELAMBAR R. KAIPATUR,<sup>1</sup> RUI ZHENG,<sup>4</sup>  
EDMOND H. LOU,<sup>3,4</sup> and PAUL W. MAJOR<sup>1</sup>

<sup>1</sup>School of Dentistry, University of Alberta, Edmonton, AB, Canada; <sup>2</sup>Department of Radiology and Diagnostic Imaging, University of Alberta, Edmonton, AB, Canada; <sup>3</sup>Department of Biomedical Engineering, University of Alberta, Edmonton, AB, Canada; and <sup>4</sup>Department of Surgery, University of Alberta, Edmonton, AB, Canada

(Received 4 February 2016; accepted 29 April 2016; published online 9 May 2016)

Associate Editor Agata A. Exner oversaw the review of this article.

**Abstract**—Intraoral ultrasonography uses high-frequency mechanical waves to study dento-periodontium. Besides the advantages of portability and cost-effectiveness, ultrasound technique has no ionizing radiation. Previous studies employed a single transducer or an array of transducer elements, and focused on enamel thickness and distance measurement. This study used a phased array system with a 128-element array transducer to image dento-periodontal tissues. We studied two porcine lower incisors from a 6-month-old piglet using 20-MHz ultrasound. The high-resolution ultrasonographs clearly showed the cross-sectional morphological images of the hard and soft tissues. The investigation used an integration of waveform analysis, travel-time calculation, and wavefield simulation to reveal the nature of the ultrasound data, which makes the study novel. With the assistance of time-distance radio-frequency records, we robustly justified the enamel-dentin interface, dentin-pulp interface, and the cemento-enamel junction. The alveolar crest level, the location of cemento-enamel junction, and the thickness of alveolar crest were measured from the images and compared favorably with those from the cone beam computed tomography with less than 10% difference. This preliminary and fundamental study has reinforced the conclusions from previous studies, that ultrasonography has great potential to become a non-invasive diagnostic imaging tool for quantitative assessment of periodontal structures and better delivery of oral care.

**Keywords**—High-frequency ultrasound, Dento-periodontium, Cemento-enamel junction, Phased array, Cone beam computed tomography (CBCT).

## INTRODUCTION

Periodontal disease is an endemic gum disease showing increasing prevalence with age and affecting up to 90% of the world population.<sup>32</sup> According to the Canadian Dental Association, one in seven middle-aged and one in three elderly people have gum disease.<sup>39</sup> Inflammation of the gums can cause detachment of gingiva from the tooth root, forming a pocket. Severe periodontitis results in eventual tooth loss due to gradual weakening and loss of tooth-supporting periodontium. Periodontal probing is one of the most common invasive methods to measure pocket depth. However, some reports indicate that inflammation of the gingiva could affect probe penetration and accuracy.<sup>23,50</sup> Furthermore, pocket depth measurement does not provide direct assessment of alveolar bone level.

Intraoral radiographs are particularly useful for determining alveolar bone level on the mesial and distal aspects of tooth roots, but do not provide information regarding alveolar bone contour on the buccal or lingual aspects of the teeth. Intraoral radiography is prone to projection errors and produces two-dimensional (2D) images that often result in overlapping anatomical structures. Buccal and lingual defects are harder to be visualized using periapical radiographs.<sup>27</sup>

Similar to a conventional medical CT scan, cone beam computerized tomography (CBCT) provides fast and accurate 3D volumetric image reconstruction and visualization of internal anatomical features<sup>5</sup> that 2D intraoral and panoramic images cannot reveal. CBCT systems have been used for maxillofacial imaging including various dental clinical applications, namely,

---

Address correspondence to Lawrence H. Le, Department of Radiology and Diagnostic Imaging, University of Alberta, Edmonton, AB, Canada. Electronic mail: lawrence.le@ualberta.ca

caries diagnosis, periodontal diagnosis, diagnosis of periapical lesions due to pulpal inflammation, visualization of pulp canals, elucidation of internal and external root resorption, and detection of root fractures.<sup>28,44</sup> CBCT currently renders the only method to visualize and analyze the bony defects on the buccal and lingual surfaces.<sup>45</sup> Despite the 3D revelation of the oral structures, the benefit of using CBCT should always be assessed against the radiation risk to patients. CBCT imaging exposes patients to a much higher dose than the intraoral and panoramic radiography.<sup>26</sup> The effective doses for dental CBCT is about 5–74 times that of a single film-based panoramic radiograph.<sup>36</sup> Furthermore, radiation exposure from repeated imaging to measure progression of bone loss due to disease or orthodontic intervention carries a radiation risk to patients due to dose accumulation. The risks are higher for pediatric patients, who have developing organs and longer lifetime for cells to develop cancer.<sup>40</sup>

Ultrasound imaging is a non-invasive and non-destructive technique used in many fields, especially in medicine and engineering. The emission of high-frequency source pulse and the detection of the echoes are accomplished by a transducer. The characteristics of the returning echoes are mainly governed by the elastic properties of the transmitting medium and the acoustic impedance contrast between the media. For decades, medical ultrasound has mainly been used to image soft tissues. In recent years, ultrasound has been utilized to study the elastic properties of hard bone tissues<sup>22,30</sup> and to image scoliotic spine.<sup>8</sup> The bone/soft-tissue interface is a strong reflector of ultrasound energy, thus making bone-tissue imaging possible. As early as 1963, Baum *et al.*<sup>3</sup> studied freshly extracted teeth using 15-MHz pulse-echo ultrasound and claimed to identify enamel-dentin and even dentin-pulp interfaces from the low-resolution primitive images. Later, Barber *et al.*<sup>1</sup> demonstrated convincing evidence to identify the interfaces and measured the hard tissue velocities. Since then, ultrasound has been explored in many fields of dentistry. Much effort has been spent to study the hard tooth tissues *in vitro* using radio-frequency (RF) signals.<sup>16,41</sup> Recently, quantitative ultrasound technique was used to evaluate stability and osseointegration of dental implant.<sup>46,47</sup> So far, imaging studies of the dento-periodontium are limited.

Fukukita *et al.*<sup>12</sup> used a single 20-MHz transducer with a mechanical driving motor to produce early B-scan images of the tooth and alveolar bone. Culjat *et al.*<sup>10</sup> performed a complete circumference scan of a human molar to obtain a primitive map of the enamel-dentin interface with a single 10-MHz transducer. Tsiolis *et al.*<sup>43</sup> employed a 20-MHz ultrasonic scanner to image the porcine periodontium. The scanner,

which was designed for dermatological use, had a single transducer translated incrementally by a motor to produce a 15-mm B-mode image of the periodontal structures. The authors compared the linear measurements between a drilled notch (in the enamel) and the alveolar crest and found the ultrasound measurements had better repeatability than the direct measurement and transgingival probing. Chifor *et al.*<sup>33</sup> also used a 20-MHz dermatological ultrasonic scanner to study pig mandibles and found accurate measurements of periodontal space width, alveolar bone thickness, and gingiva. Their scanner had a single transducer, mounted in a 2D scanning hand-held probe. The authors also found significant correlations for alveolar bone level measurements among ultrasound, CBCT, and light microscopy. Salmon and Le Denmat<sup>34</sup> developed a 25-MHz ultrasound prototype system with a single 3.6-mm diameter transducer to perform ultrasound examinations on healthy volunteers. The transducer was linearly translated with a 10-Hz scanning motion. The acquired images showed the cementum and also the alveolar process. Most recently, Zimbran *et al.*<sup>52</sup> provided periodontal structures of human premolars *in vivo* using 40 MHz with a commercial SonoTouch ultrasound scanner (Analogic, Vancouver, Canada) equipped with an array transducer. While the feasibility of using ultrasound to study dento-periodontal tissues has been somewhat confirmed, the ultrasound images published so far lack the quality and clarity, and the accuracy of the ultrasound method has not been adequately established. Most recently, Nguyen *et al.*<sup>29</sup> used a 20-MHz transducer to image the cementum-enamel junction (CEJ) of six porcine lower central incisors. The study found the measured distances between the CEJ and a referenced notch from the ultrasound and micro-CT images had strong correlation and agreed up to 97%, where the micro-CT measurements are considered a benchmark for *ex vivo* accuracy measurements.

This study is different from our previous study<sup>29</sup> published recently in two main aspects. First, a commercial medical ultrasound system with a multi-element array transducer was used instead of a mechanically translated single transducer. The ultrasound scanner significantly sped up the data acquisition process, acquired quality data with good signal-to-noise ratio (SNR), and provided a real-time high-resolution image of the periodontal structures. Secondly, the ultrasound measurements were compared with those of current clinically available CBCT imaging technology. Although there are numerous studies investigating the validity and accuracy of CBCT to identify and measure periodontal structures and disease status as discussed in a recent systematic review,<sup>48</sup> CBCT imaging is still not considered a gold standard



**FIGURE 1.** A porcine mandible with four teeth from a 6-month-old piglet: right lateral incisor (RLI), right central incisor (RCI), left central incisor (LCI), and left lateral incisor (LLI).

for periodontal imaging as it provides a high hard tissue contrast but poor soft tissue contrast.<sup>36,37</sup> It is mostly used as an adjunct to other clinical assessment techniques.<sup>11,20</sup>

Hence, the objectives of the present investigation are to utilize a medical ultrasonic array system to image hard dental tissues and periodontal attachment apparatus, and to compare the level of agreement between ultrasound measurements with those of CBCT imaging. In addition, principles of ultrasound propagation and wavefield simulation are used to analyze the reflection events associated with dento-periodontal tissues.

## MATERIALS AND METHODS

### *Preparation of Sample*

The sample had four lower incisors from a freshly harvested mandible of a 6-month-old piglet (Fig. 1), which was raised in the university animal farm (University of Alberta). The piglet was originally euthanized to conduct experiments by the nutrition research group and the mandible was kindly donated after use. The mandible was shaved, cleaned, and then frozen, waiting for the availability of the CBCT scanner. We used the right central incisor (RCI) and left central incisor (LCI) for the imaging experiments.

### *CBCT Imaging*

The frozen mandible was scanned by an i-CAT 17-19 high resolution dental CBCT system (Imaging Sciences International, Hatfield, PA, USA) (Fig. 2a). The scanner has amorphous silicon flat panel sensor with

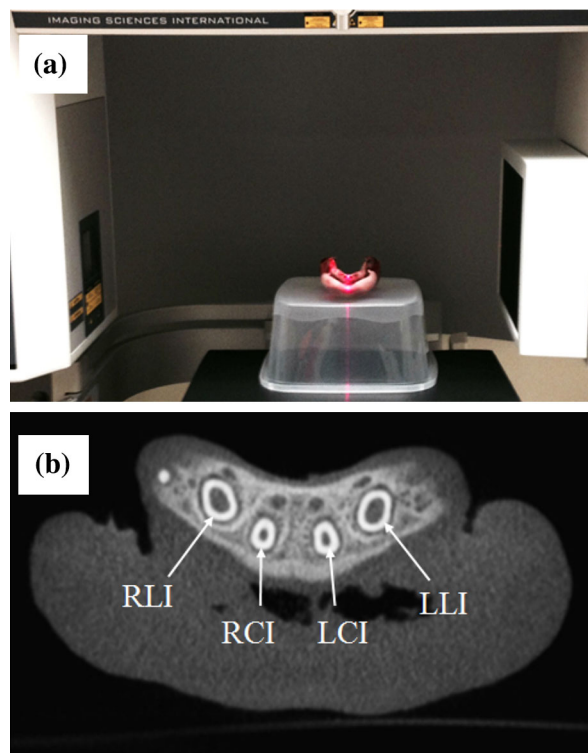


**FIGURE 2.** A CBCT scan: (a) Mandible centered in the gantry with the assistance of the positioning laser beams and (b) a coronal image of the mandible showing four incisors.

Cesium Iodide (CsI) scintillator material to enhance SNR and image quality, voxel size ranging from 0.125 to 0.40 mm, scanning time from 5 to 26.9 s for small to large FOV, and 14-bit gray scale resolution. The collimation is electronically controlled to ensure the focusing of the radiation field on the region of interest (ROI). For this study, high resolution imaging was performed with a 0.2-mm voxel, 26.9 s scanning, and 16 cm × 6 cm FOV. The image of the four incisors, extracted from a CBCT coronal projection of the mandible, is shown in Fig. 2b.

### *Ultrasound Imaging*

We used a portable diagnostic SonixTablet ultrasound phased array system (Analogic, Vancouver, BC, Canada). The scanner has a fully programmable 19" high resolution touch screen (Fig. 3a) to choose the imaging parameters such as frequency, time gain compensation, depth, and dynamic range. The transducer used is a broadband 8–40 MHz array transducer (L40-8/12, Analogic, Vancouver, BC, Canada) with 128 (0.1-mm pitch) elements (Fig. 3b). The transducer, which was designed specifically for musculoskeletal and peripheral vascular exams, has a small 13 mm × 4 mm footprint.



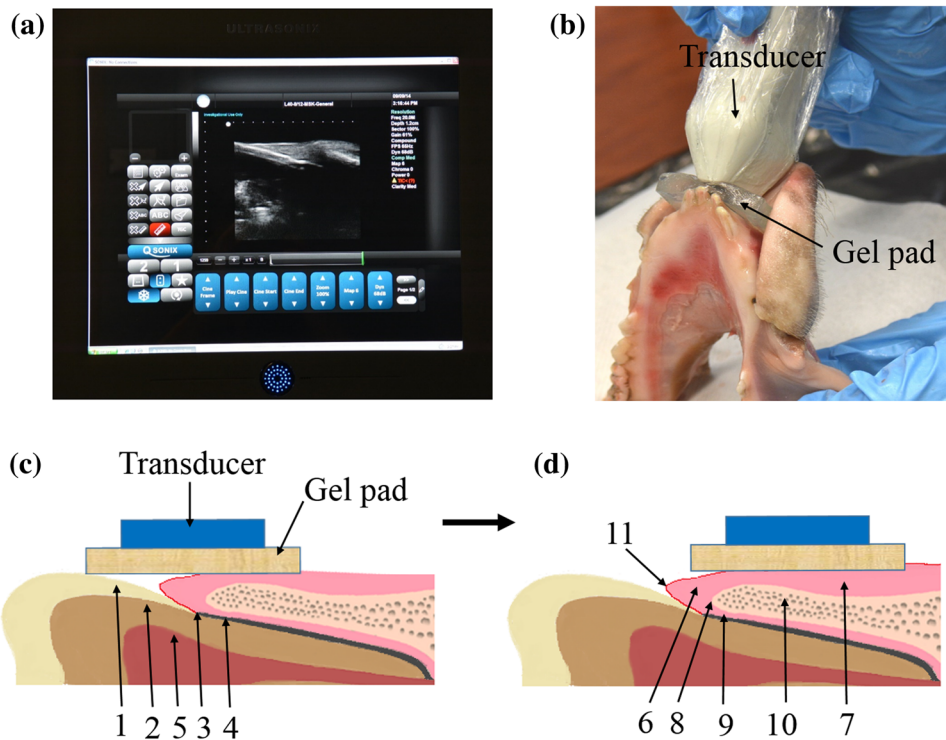


**FIGURE 3.** Ultrasound experiment: (a) The touch-screen SonixTablet ultrasound phased array system and (b) the 128-element L40-8/12 transducer (Analogic, Vancouver, Canada) positioned to scan the LCI. The artistic images show (c) the original position of the transducer straddling across the tooth and the gingiva, and (d) the final position of the transducer on top of the gingiva. Numeric annotations indicate (1) enamel, (2) dentin, (3) cemento-enamel junction, (4) cementum, (5) pulp chamber, (6) gingiva, (7) alveolar mucosa, (8) alveolar crest, (9) periodontal ligament, (10) alveolar bone, and (11) gingival margin.

The resolution parameters of the ultrasound beam were determined by scanning a multi-general ultrasound ATS 549 phantom (ATS Laboratories, Bridgeport, CT, USA). The cylindrical targets were made up of the monofilament nylons with a 0.12-mm diameter.

The imaging experiments were performed on the piglet's mandibular incisor periodontium using a 20-MHz ultrasound beam at 20 °C room temperature. The transducer was positioned to straddle the tooth and gingiva on the labial side with the long axis of the transducer in alignment with the longitudinal axis of the tooth (Fig. 3b). A piece of 4 mm thick gel coupling, prepared from a commercial Aquaflex ultrasound gel pad (Parker Laboratories Inc., Fairfield, NJ, USA), was placed between the contact areas to achieve good coupling. The gel pad (GP) also placed the ROI within the focal zone of the ultrasound beam, which ensured optimum resolution<sup>51</sup> and delayed the pulse to image the enamel and gingival surfaces. Ultrasound gel (Aquasonic 100, Parker Laboratories, Inc., Fairfield, NJ, USA) was used to fill in any void or gap between contacting surfaces. During scanning, the transducer was slid longitudinally from top to the bottom of the incisors, i.e., from left (Fig. 3c) to right (Fig. 3d) as shown in the schematic diagrams. The end position of the transducer was on the top surface of the gingiva with the

alveolar process underneath it (Fig. 3d). Each ultrasound image has a vertical depth axis and a horizontal axis indicating the position of channel or record (POR). The PORs are measured with respect to the position of the first element, which is zero. All the images were recorded as video clips with a 27-Hz frame rate for 10–15 s and exported to a desktop for further analysis.

#### Wavefield Simulation

Partition of energy occurs when ultrasound encounters a tissue interface. The reflected and transmitted amplitudes of the signals, for a normal incident ultrasound beam, are governed by the reflection coefficient,  $R$  and transmission coefficient,  $T$  respectively, i.e.,

$$R_{12} = \frac{Z_2 - Z_1}{Z_2 + Z_1} \text{ and } T_{12} = \frac{2Z_2}{Z_2 + Z_1} \quad (1)$$

with the corresponding intensities

$$I_R = \left( \frac{Z_2 - Z_1}{Z_2 + Z_1} \right)^2 \text{ and } I_T = \frac{4Z_2Z_1}{(Z_2 + Z_1)^2} \quad (2)$$

where  $Z_1$  and  $Z_2$  are the impedances of the media traversed by the incident and transmitted beams respectively. The densities and the speeds of sound for

**TABLE 1. Densities and acoustic properties of the dental hard and soft tissues in human and gel pad.**<sup>10,13</sup>

Material	Speed of sound (ms <sup>-1</sup> )	Density (kg m <sup>-3</sup> )	Acoustic Impedance (10 <sup>6</sup> Rayl)
Gel pad	1480	1000	1.48
Gingiva <sup>13</sup>	1540	1060	1.63
Enamel <sup>10</sup>	5700	2900	16.5
Dentin <sup>10</sup>	3800	2100	8.0
Pulp <sup>13</sup>	1570	1000	1.57
Cementum <sup>13</sup>	3200	2030	6.5

**TABLE 2. Reflection and transmission coefficients and intensities.**

Interface	$R_{12}$	$T_{12}$ ( $T_{21}$ *)	$I_R$ (%)	$I_T$ (%)
Gel pad - Gingiva	0.05	1.05 (0.95)	0.23	99.77
Gel pad - Enamel	0.84	1.84 (0.16)	70	30
Gingiva - Enamel	0.82	1.82 (0.18)	67	33
Gingiva - Cementum	0.60	1.60 (0.40)	36	64
Enamel - Dentin	-0.35	0.65 (1.35)	12	88
Dentin - Pulp	-0.67	0.33 (1.67)	45	55

\*  $T_{21}$  is given by  $2Z_1/(Z_2 + Z_1)$ .

different human dental hard and soft tissues are listed in Table 1 along with the corresponding acoustic impedances, which are given by the products (density  $\times$  velocity). The properties of the gel pad are similar to those of water. Table 2 lists the corresponding reflection and transmission coefficients and intensities.

Wavefield modeling is a powerful tool to simulate or predict wavefield response to help interpret the dental structures in the B-mode image. Simulation was performed by means of a convolution operation,

$$s(t) = I_R(t) * w(t) \quad (3)$$

where  $*$  is the convolution operator,  $I_R$  is the reflectivity of the structure, and  $w(t)$  is the source wavelet. The wavelet used in this context is an oscillatory signal. Equation (3) only considers the primary reflectivity or reflections within the layers. The primary reflectivity consists of a series of impulses at the locations of the interfaces. The product of the amplitude transmission coefficients (when the wavelet crosses the interfaces) and the amplitude reflection coefficient (when the reflector reflects the wavelet) gives the strength and polarity of each impulse. The location of the impulse is determined by the sum of the two-way normal travel times within the layers between the reflector and the transducer.

We should mention that the simulation study was solely used in this fundamental investigation to identify some of the reflectors observed in the ultrasound B-mode images. The RF waveforms were not meant to be used in a clinical setting.

## RESULTS

Figure 4a shows the normalized RF signals reflected by a target at 8 mm below the scanning surface of a multi-general ultrasound ATS 549 phantom. The signals were normalized by the global maximum absolute value within the indicated time-position ( $t - x$ ) panel of interest, which spans from 9.5 to 11.5  $\mu$ s and from 7 to 8.6 mm POR to cover 33 records. The spacing,  $\Delta x$ , between the RF signals is 0.05 mm. The reflected energy from a cylindrical target was not localized but spread across the image, which more or less shows the line spread function of the imaging system. To estimate the lateral resolution, we chose the eleven records with the maximum absolute amplitude greater than 50% and estimated a resolution of 0.5 mm (0.05 mm  $\times$  10). The SonixTablet also has dynamic focusing capability to extend the lateral resolution below and above the focal depth. We examined a dominant pulse from a normalized RF time series at 7.75 mm POR (Fig. 4b). The temporal pulse length (TPL) was determined to be 0.25  $\mu$ s with 2.5 cycles based on the absolute amplitude greater than 35% of the maximum. The spatial pulse length (SPL) is  $TPL \times v$  where  $v$  is the ultrasound velocity of the transmitting material. Considering 1500 ms<sup>-1</sup> to be the velocity for the tissue-mimicking material, the SPL was 0.375 mm. The axial resolution (AR), which measures the minimum separation between two reflectors to prevent the echoes from these two reflectors from overlapping, was given by  $SPL/2$  or 0.19 mm.<sup>7</sup> Using 1564 ms<sup>-1</sup> as the velocity for the porcine gingiva,<sup>38</sup> the AR was 0.20 mm.

A B-mode image of the RCI is shown in Fig. 5. Two frames from the video clip were manually stitched together using three distinct points within the images to illustrate a longer image of 18 cm. The small area symmetrically enclosing the stitching line (approximately  $50 \times 200$  pixels) was smoothed by a two-pass 2D  $3 \times 3$  (9 pixels) averaging filter. The averaging operation, which was used to smooth the joint of the two stitched images, was not used in real time imaging.

The enamel (#1) and cementum (#4) are strong ultrasound reflectors and can be easily identified. The dentin (#2) reflector, which cannot be resolved from

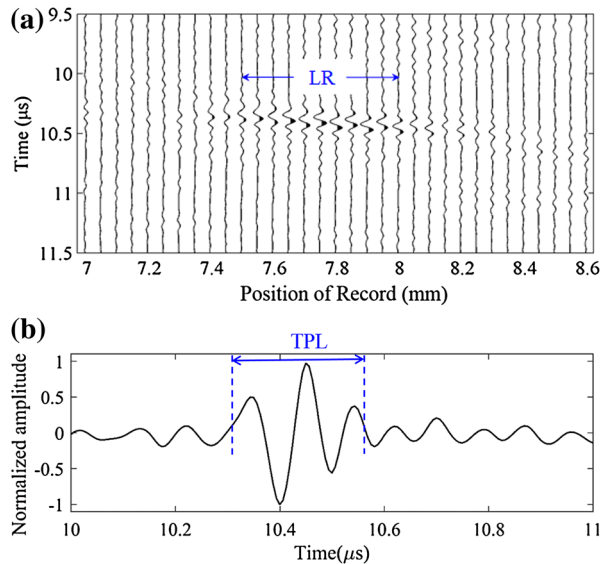


**FIGURE 4.** Resolution measurements from an ultrasound ATS 549 phantom: (a) Lateral resolution and (b) temporal pulse length (TPL). The measurements were made at 20 MHz and 8 mm focal depth. The lateral resolution is  $0.05 \text{ mm} \times 10 = 0.5 \text{ mm}$ . The TPL, based on the time record at 7.75 mm POR, is  $0.25 \mu\text{s}$ .

the enamel, merge with enamel at the CEJ (#3), and continues into the root underneath the cementum (#4). Since ultrasound cannot penetrate efficiently through the alveolar bone to the cementum below, the echoes coming from the underlying cementum are quite weak. Therefore, the location of the alveolar crest (#8) is considered to be close to where the cementum reflection ends. Using these interfaces as reference, we can identify gingival margin (#11), gingiva (#6), alveolar mucosa (#7), and periodontal ligament (or space) (#9). We chose to measure the linear distance between the gingival margin and CEJ (A), the distance between the gingival margin and alveolar crest (B), and the thickness of crestal alveolar bone (C) (Fig. 6). These landmarks are commonly used to determine periodontal structures and its disease progression. Periodontal disease progression is associated with gradual loss of supporting structures of the tooth, namely, the gingiva, periodontal ligament, and alveolar bone. Measuring the distance from these structures to a standard reference point on the tooth surface such as CEJ, that does not alter with disease progression, helps to measure and monitor periodontitis accurately.<sup>6,18</sup> The measurements were performed on the ultrasound and CBCT images three times by two observers, with 3 days interval between measurements. The Matlab (version R2013a, MathWorks, Natick, MA, USA) software was used to convert the ultrasound images to DICOM format. The RadiAnt DICOM Viewer (version 1.9.16, Medixant, Poland) was then used to perform the measurements in the sonographs and CBCT images. Both raters yielded small variations of the measurements for the two methods (Table 3). The percentage differences between ultrasound and CBCT measurements for A, B, and C are, on the average, 3.8, 7.9, and 9.1% for rater 1 and 2.8, 9.8, and 6.9% for

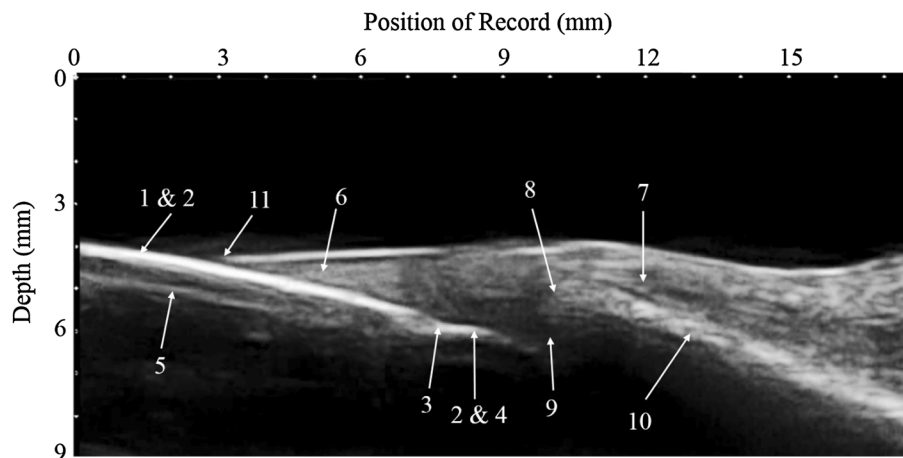


**FIGURE 5.** A 20-MHz ultrasonic B-mode image of the right center incisor (RCI). Numeric annotations indicate (1) enamel, (2) dentin, (3) cemento-enamel junction, (4) cementum, (5) dentin-pulp reflector possibly overlapped by source-induced multiple reflections, (6) gingiva, (7) alveolar mucosa, (8) alveolar crest, (9) periodontal ligament, (10) alveolar bone, and (11) gingival margin.

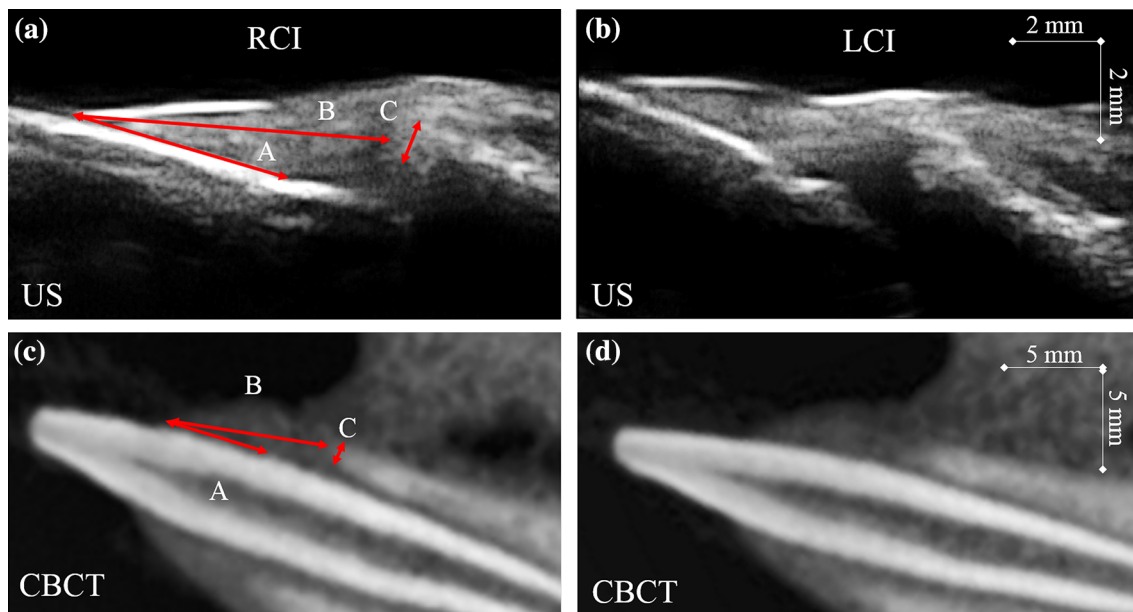


**FIGURE 6.** Ultrasound (US) and CBCT images of the teeth and periodontium. The left panel is for the RCI: (a) the ultrasonic B-mode image and (c) the CBCT image. The corresponding images for the LCI are shown in (b) and (d). The arrows (in red) indicate the distance from gingival margin to cemento-enamel junction (A), the distance between gingival margin and alveolar crest (B), and the thickness of the alveolar bone at the crest (C).

**TABLE 3.** Comparison of measurements between ultrasound (US) and CBCT of the two incisors for two raters, R1 and R2.

Quantity	$\bar{D}_{US} \pm SD_{US}$ (mm)	$\bar{D}_{CBCT} \pm SD_{CBCT}$ (mm)	MAD (mm)	PD (%)
<i>RCI</i>				
R1				
A	4.993 ± 0.087	5.060 ± 0.094	0.067	1.3
B	7.472 ± 0.149	8.060 ± 0.155	0.588	7.6
C	0.840 ± 0.051	0.919 ± 0.039	0.079	9.0
R2				
A	4.962 ± 0.090	5.034 ± 0.173	0.072	1.4
B	7.565 ± 0.067	8.331 ± 0.071	0.765	9.6
C	0.817 ± 0.072	0.887 ± 0.058	0.071	8.3
<i>LCI</i>				
R1				
A	4.663 ± 0.414	4.962 ± 0.038	0.299	6.2
B	7.331 ± 0.315	7.955 ± 0.377	0.624	8.2
C	0.791 ± 0.043	0.866 ± 0.120	0.076	9.1
R2				
A	4.632 ± 0.061	4.829 ± 0.091	0.197	4.2
B	7.093 ± 0.069	7.833 ± 0.131	0.740	9.9
C	0.786 ± 0.015	0.830 ± 0.065	0.044	5.4

The annotations follow Fig. 5: the distance from gingival margin to cemento-enamel junction (A), the distance between gingival margin and alveolar crest (B), and thickness of the alveolar bone at the crest (C).  $\bar{D}$  and SD stand for the mean and standard deviation of the measurements. MAD denotes the mean absolute difference between the two methods, i.e.,  $|\bar{D}_{CBCT} - \bar{D}_{US}|$  and the percentage difference (PD) is given by  $\frac{MAD}{\frac{\bar{D}_{CBCT} + \bar{D}_{US}}{2}} \times 100$ .

rater 2 respectively with ultrasound underestimating all values.

## DISCUSSION

In this study, we attempted to use a broadband multi-element array transducer to image the incisors

and the surrounding periodontium. To our knowledge, this is the first study to investigate quantitatively the periodontal tissues including the alveolar bone in the lower anterior mandibular region using an array transducer and compare with clinical CBCT measurements. The use of swine as an ideal model for dental research is justified because its dentition and oral



function bear close resemblance to human's.<sup>49</sup> The human enamel is thicker compared to swine enamel, but the enamel and dentin structures are very similar in both human and swine.<sup>24</sup> The ultrasound speed of porcine gingiva is  $1564 \text{ ms}^{-1}$ ,<sup>38</sup> very close to  $1540 \text{ ms}^{-1}$  of human gingiva. The ultrasound speeds of other porcine hard tissues are not known and were approximated to those of human.

The transducer used was designed for medical soft-tissue imaging but the footprint and element size were small enough for us to consider for the intraoral experiments. The transducer has a broad operating frequency range from 8 to 40 MHz. Zimbran *et al.*<sup>52</sup> used a similar transducer in their study. Several operating frequencies (10–35 MHz)<sup>10,15,16</sup> have been used to evaluate enamel thickness with single transducers. Most research groups used 20 MHz to do periodontal ultrasonography on pig periodontium.<sup>25,43</sup> Recently Salmon and Denmat<sup>34</sup> used 25-MHz ultrasound beam on human subjects. We chose to use 20 MHz for this research to be compatible with other studies and struck a compromise between resolution, imaging noise, and penetration depth. The scanner used all 128 elements and electronically delayed them to generate a focused ultrasound beam on a targeted area at fixed location and focal depth. The echoes of the focused beam were recorded as a RF time series, which was processed to create an A-scan. Then the scanner swept the beam across the focal depth to generate a B-mode frame (or image) of the target. Our images have 256 scan lines (or time series) per frame by means of compound imaging and have much superior image quality and clarity than those reported in the current literature, especially from those acquired using a single transducer.<sup>9,25,43</sup> The use of array transducer also reduced the data acquisition time to less than 15 s (excluding the time to save the images after scanning), avoiding any patient motion errors and potentially benefiting the practitioner in decreasing practitioner's chair time. By using a phased array transducer, we eliminated another challenge associated with the use of single transducer, minimizing the effort to position the transducer incrementally and accurately even with a scanning motor mechanism.

Hard tissue such as enamel has much larger acoustic impedance than that of the gel pad and gingiva, resulting in large impedance contrast. The ultrasound beam, incident upon the gel pad-enamel (GPE) or gingiva-enamel (GE) interface, underwent specular reflection and the echoes were hyper-echoic signals carrying about 67–70% of the incident energy (Table 2), as evidenced by the enamel reflector (#1) in Fig. 5. There was also a visible reflection at 4 mm depth and between 3 and 7.8 mm POR. The reflector

was the attached gingiva, where the tissue was harder due to keratinization. The mucogingival junction was around 8 mm POR and 4 mm depth, separating the attached keratinized gingiva and non-keratinized mucosa. Non-keratinized mucosa or alveolar mucosa was the unattached mucosa. It was less dense than the attached gingiva, and thus did not reflect as much ultrasound energy as the attached gingiva. Only 12% of the transmitted energy through enamel was reflected by the enamel-dentin (ED) interface.

To explore the ED reflection further, we examined the RF data of the RCI. The  $t - x$  RF waveforms shown in Fig. 7 display the reflections corresponding to the reflectors in Fig. 5 between 1.5 and 8.7 mm POR. Using the first time series at 1.5 mm POR for the computational analysis, the GPE reflection was around  $5.7 \mu\text{s}$ . The thickness of enamel,  $h_{\text{enamel}}$ , was 0.45 mm estimated from the CBCT image (Fig. 6c). Based on the two-way travel time within the enamel layer,

$$t_{\text{enamel}} = 2 \times h_{\text{enamel}} / v_{\text{enamel}}$$

where  $v_{\text{enamel}} = 5700 \text{ ms}^{-1}$  is the ultrasound velocity of enamel (Table 1), the arrival of the ED echo was  $5.86 \mu\text{s}$  or approximately  $0.16 \mu\text{s}$  later than the GPE echo. Since the axial resolution of the transmitted pulse was roughly 0.71 mm in enamel, the ultrasound beam could not resolve the 0.45 mm thick enamel layer and thus the GPE and ED echoes overlapped, resulting in complicated waveforms. There is a small reflection event around  $6.65 \mu\text{s}$ , which we suspected to be the dentin-pulp (DP) reflection. To verify our speculation, we started out to calculate the thickness of dentin bounded by the ED and DP reflections based on their arrival times,  $t_2$  and  $t_3$  by

$$h_{\text{dentin}} = v_{\text{dentin}} \times (t_3 - t_2) / 2$$

where the denominator 2 converts the two-way travel time to one-way travel time and  $v_{\text{dentin}}$  is the ultrasound speed of dentin. Using  $v_{\text{dentin}} = 3800 \text{ ms}^{-1}$  (Table 1), the dentin was estimated 1.5 mm thick, comparable to the approximate measurement of 1.4 mm from CBCT image. Therefore, the echo from the DP interface should arrive around  $6.65 \mu\text{s}$ . However, the energy of this echo was just 3% of the incident energy, which might be under the noise level to be observable. The DP reflection was identified as early as 1963.<sup>1,3</sup> There were internal multiple reflections within the matching layer of the transducer. These multiples created secondary source signals traveling through the tissues and interacted with the tissue interfaces, similar to the primary source signal. The first source-induced multiple reflections are approximately  $1 \mu\text{s}$  apart from the primary ED reflections, resulting in artefacts in the



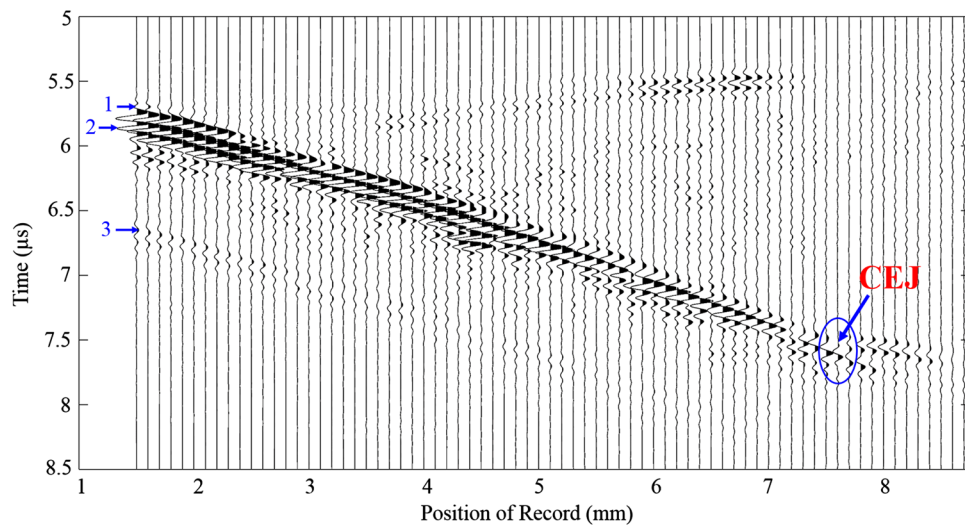


**FIGURE 7.** The RF waveforms of the RCI data. The time signals show the reflections from the enamel (1) and the dentin (2). The reflection from the pulp chamber (3) coincides with the source-induced multiple reflections. The circle shows the area where the enamel and dentin merge and the arrow points to the approximate location of the CEJ around  $7.5 \mu\text{s}$  and  $7.6 \text{ mm}$ .

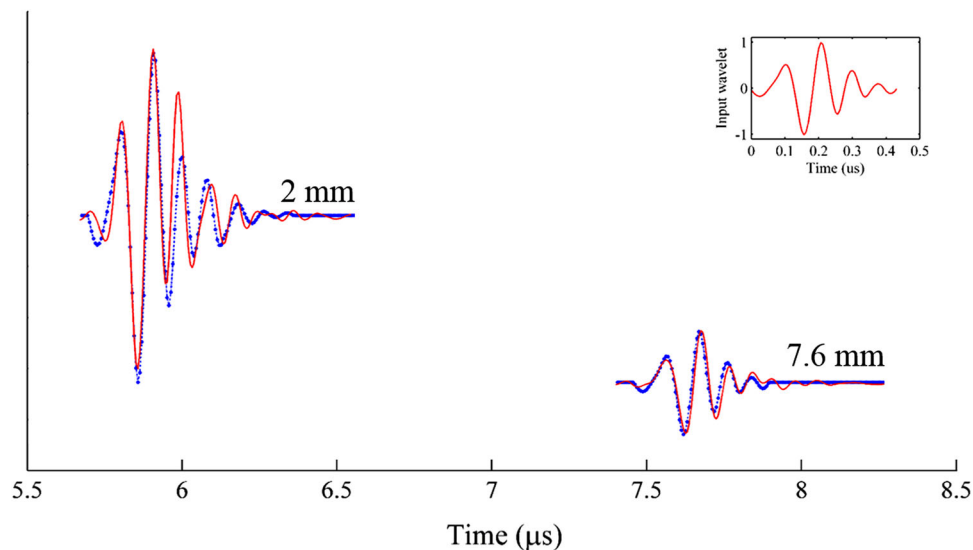


**FIGURE 8.** A comparison of the simulated and real signals at two locations. The simulated signals were computed by convolving the source wavelet (shown in inset) with the reflectivity impulse(s) of the interface(s) at each location. (red: real data and blue: simulated data).

image. In this case, these multiples arrived at about the same time as the DP echo, which corresponds to the location of reflector #5 in Fig. 5.

The CEJ is the intersection between the enamel, which covers the crown of a tooth, and the cementum, which covers the root. The CEJ is an important marker to diagnose gingival recession, alveolar bone loss, and clinical attachment level in periodontal disease.<sup>29</sup> Due to lack of resolution, we found it difficult to identify the CEJ in the CBCT images without proper windowing and leveling. The enamel layer became thinner

toward the direction of CEJ and eventually terminated when the junction was reached. The location of CEJ was usually recognized as a depression due to a delay in arrival time. Correspondingly, the complicated waveforms (Fig. 7) became much simpler with fewer cycles or oscillations as the junction was approached around  $7.6 \text{ mm}$  POR and  $7.5 \mu\text{s}$  (Fig. 7). Because the cementum layer was very thin at the junction, the reflections from the gingiva-cementum and cementum-dentin interfaces had very small time delays and were completely overlapped.

To explore the previously identified (GPE and ED) reflection events and the location of CEJ further beyond the travel-time method, we simulated the waveforms (Fig. 8) by means of convolution. The temporal locations of the reflectivity impulses at each location were estimated from the RF signals (Fig. 7). Two POR locations (2 and 7.6 mm) were considered. At 2 mm POR, there were two impulses with the first impulse accounting for the GPE reflection and the second impulse for the transmission across the GPE interface twice (one down and one up) and the enamel-dentin reflection. As the POR increased, the enamel became thinner and thus the GPE and ED interfaces or reflectivity impulses were closer. At 7.6 mm POR where the CEJ was, the two impulses merged into a single gingiva-cementum reflectivity impulse, which accounted for the back-and-forth transmission across the gel pad-gingiva interface and a gingiva-cementum reflection. The source signal was the wavelet we used to determine the axial resolution of the beam (Fig. 5b) but was  $0.17 \mu\text{s}$  longer ( $0.42 \mu\text{s}$  in total length) with 4.5 cycles, which was deemed necessary to provide a detailed match with the real signals. This source wavelet had finite energy and zero mean. The simulated signals at two locations compared well with the real signals, confirming our previous identification of the enamel and dentin reflectors and the location of CEJ. The simple convolution model, which considers a constant source wavelet convolving with the closely spaced reflectivities without the inclusion of internal scattering, seems to be adequate in this case; however, full wavefield simulation using finite element or finite difference would be a more appropriate approach to model ultrasound interaction with the tooth tissues.

The interaction of ultrasound with alveolar cancellous bone is complicated. The bone surfaces were irregular and non-specular with porosity. Ultrasonic attenuation of alveolar bones<sup>17</sup> has not been well studied, however, research findings relevant to cancellous bones (e.g., Ref. 30) can be qualitatively applied here to explain the data. Scattering and absorption contribute to ultrasound attenuation. Scattering results from the interaction of ultrasound with the structural inhomogeneity of the tissues and the tissue boundaries. Scattering from the roughness of the boundaries increases with frequency.<sup>7</sup> Energy is randomly scattered away from the main directivity of the transducer, causing an apparent attenuation of the signal. Scattering was found to be a dominating mechanism of attenuation in cancellous bones when wavelength of the signal is large compared to the size of the scatterer.<sup>31</sup> High frequency ultrasound provides better axial resolution but also receives much scattered energy from the inhomogeneity of the soft tissues, which tends to make the image noisy. The 40-MHz

ultrasound images from Zimbran *et al.*<sup>52</sup> illustrated such a case. Due to scattering, the reflection from alveolar bones is less focused and remains blurred. The gingiva-alveolar bone interface is a good example. The interface was ill defined and appeared as a zone of finite thickness, which might not represent the true thickness of the alveolar bone because ultrasound basically could not penetrate deeply into bone tissue. The same phenomenon was observed by Chifor *et al.*<sup>9</sup> and Salmon and Le Denmat.<sup>34</sup> The fuzziness of the interface was the main source of error when we did the dimensional measurement involving alveolar bone. In our study, the measurements between the two methods for the distance parameter A, gingival margin to CEJ, agreed within 3.8%; however, with respect to distance measurements from the alveolar bone, the discrepancies were larger, but within 10% for parameter B (the distance between gingival margin and alveolar crest) and parameter C (the thickness of the alveolar bone at the crest) respectively. The percentage differences between ultrasound and CBCT measurements showed that ultrasound underestimated the measurements in comparison to CBCT (Table 3). Hefti *et al.*<sup>14</sup> quotes that “in order to provide useful information about measurement error, it must be judged against a familiar error source”. Since CBCT is not considered the gold standard in periodontal imaging,<sup>11,20,36</sup> it is noteworthy to speculate here that the true value for all three parameters might actually be in between the values obtained for both ultrasound and CBCT, thereby decreasing the amount of error in ultrasound measurements. Even if we hypothetically consider that the true value to be close to CBCT measurement, the error in underestimating using ultrasound was within 10%, with a maximum value of 0.765 mm for parameter B (gingival margin to alveolar bone crest). This error is insignificant when taken into consideration the actual distance measured, other sources of error for measuring, and its significance in monitoring periodontal disease progression.

Absorption mechanism not only dissipates energy of the ultrasound beam as heat but also removes preferentially high frequency components of the beam, causing the pulse to become broader.<sup>21</sup> The pulse-broadening effect decreases the imaging resolution of the beam. Acoustic absorption usually increases with frequency<sup>42</sup> and places a limitation to depth penetration of the ultrasound signal. The poor penetration of ultrasound energy through the alveolar bone made the identification of the underlying PDL and cementum reflector further away from the alveolar bone crest difficult. Lost *et al.*<sup>25</sup> recognized the cancellous bone (bony plate) as the essential limiting factor to prevent the identification of the periodontal space in the ultrasound images.

The thickness of the gingiva can affect surgical treatment planning and outcomes because the thick and thin gingival biotype responds differently to inflammation, restorative trauma, orthodontic insult, and surgical injury.<sup>19</sup> Identification of the periodontal biotype is essential for an optimal planning of preventive and therapeutic management.<sup>4</sup> More precise transgingival probing with local anesthesia is a common invasive method.<sup>35</sup> Another non-invasive method involves CBCT.<sup>2</sup> Slak *et al.*<sup>38</sup> assessed the gingival thickness using 50-MHz ultrasound and found the results accurate for the assessment of periodontal biotype. In our experiment, the gingiva and alveolar mucosa were clearly seen in the ultrasound images and their thickness could unambiguously be measured. Ultrasound has been used for decades to image soft tissues in diagnostic imaging and hence the results thus found were not surprising.

The application of ultrasound to image dento-periodontal tissues is a challenging problem. The imaging problem involves inhomogeneous soft tissue and cancellous bone, which are highly scattering tissues. The attempt to resolve features of soft and hard dental tissues requires different wavelengths because the speed of the dental tissues ranges from  $1540 \text{ ms}^{-1}$  (gingiva) to  $5700 \text{ ms}^{-1}$  (enamel). As discussed previously, increasing frequency has the benefit of increasing imaging resolution but also the disadvantages of decreasing image contrast due to scattering and increasing the attenuation of the ultrasound as it penetrates through hard tissues and alveolar bone, thus reducing the penetration depth.

## CONCLUSION

We investigated the use of a commercial medical ultrasound phased array system with a 128-element array transducer to scan the porcine periodontium. With 20-MHz ultrasound, the 2-cm long cross-sections of the incisors were obtained. The images show clearly the major hard tissue interfaces and the surrounding periodontium with the exception of the tissues underneath the alveolar bone. Using the RF signals as complements to the ultrasound images, the reflections from the enamel-dentin interface, the dentin-pulp interfaces and the cemento-enamel junction were identified by an integration of waveform analysis and travel-time computation, which was novel in the study. To our knowledge, this is the first report to present high-quality ultrasound images of the tooth and the surrounding periodontium and use a combination of ultrasound physics, travel-time computation, and wavefield simulation to interpret the results with

comparison to the CBCT measurements. The differences between ultrasound and CBCT measurements are within 10%. The outcomes of this study have demonstrated that ultrasound has great potential to become a non-invasive diagnostic imaging tool to assess periodontal structures and to deliver a significant impact in the practice of dentistry with less ionizing radiation and better oral care. Image processing techniques are considered necessary to enhance the coherence signals and signal-to-noise ratio for the delineation of alveolar bone reflections, which might help visualize and outline the alveolar crest better. Investigation for an optimal imaging frequency and further confirmation of the ultrasound technique by comparing more *ex vivo* measurements with direct probing, CBCT, and micro-CT measurements should be further explored as a precursor to *in vivo* clinical human study. These will be the goals of our future research.

## REFERENCES

- <sup>1</sup>Barber, F., S. Lees, and R. Lobene. Ultrasonic pulse-echo measurements in teeth. *Arch. Oral Biol.* 14:745–760, 1969.
- <sup>2</sup>Barriviera, M., W. R. Duarte, A. L. Januário, J. Faber, and A. C. B. Bezerra. A new method to assess and measure palatal masticatory mucosa by cone-beam computerized tomography. *J. Clin. Periodontol.* 36:564–568, 2009.
- <sup>3</sup>Baum, G., I. Greenwood, S. Slawski, and R. Smirnow. Observation of internal structures of teeth by ultrasonography. *Science* 139:495–496, 1963.
- <sup>4</sup>Bednarz, W. The thickness of periodontal soft tissue ultrasonic examination-current possibilities and perspectives. *Dent. Med. Probl.* 48:303–310, 2011.
- <sup>5</sup>Bornstein, M. M., R. Lauber, P. Sendi, and T. von Arx. Comparison of periapical radiography and limited cone-beam computed tomography in mandibular molars for analysis of anatomical landmarks before apical surgery. *J. Endod.* 37:151–157, 2011.
- <sup>6</sup>Brown, L. J., and H. Løe. Prevalence, extent, severity and progression of periodontal disease. *Periodontol* 2000(2):57–71, 1993.
- <sup>7</sup>Bushberg, J. T., and J. M. Boone. *The Essential Physics of Medical Imaging*, Chapter 14. Philadelphia: Lippincott Williams & Wilkins, 2011.
- <sup>8</sup>Chen, W., E. H. Lou, P. Q. Zhang, L. H. Le, and D. Hill. Reliability of assessing the coronal curvature of children with scoliosis by using ultrasound images. *J. Child. Orthop.* 7:521–529, 2013.
- <sup>9</sup>Chifor, R., M. Hedesiu, P. Bolfa, C. Catoi, M. Crisan, A. Serbanescu, A. F. Badea, I. Moga, and M. E. Badea. The evaluation of 20 MHz ultrasonography, computed tomography scans as compared to direct microscopy for periodontal system assessment. *Med. Ultrason.* 13:120–126, 2011.
- <sup>10</sup>Culjat, M., R. S. Singh, D. Yoon, and E. R. Brown. Imaging of human tooth enamel using ultrasound. *IEEE Trans. Med. Imaging* 22:526–529, 2003.

- <sup>11</sup>Du Bois, A., B. Kardachi, and P. Bartold. Is there a role for the use of volumetric cone beam computed tomography in periodontics? *Aust. Dent. J.* 57:103–108, 2012.
- <sup>12</sup>Fukukita, H., T. Yano, A. Fukumoto, K. Sawada, T. Fujimasa, and I. Sunada. Development and application of an ultrasonic imaging system for dental diagnosis. *J. Clin. Ultrasound* 13:597–600, 1985.
- <sup>13</sup>Ghorayeb, S. R., C. A. Bertoncini, and M. K. Hinders. Ultrasonography in dentistry. *IEEE Trans. Ultrason. Ferroelect. Freq. Control* 55:1256–1266, 2008.
- <sup>14</sup>Hefti, A. F., and P. M. Preshaw. Examiner alignment and assessment in clinical periodontal research. *Periodontol* 2000(59):41–60, 2012.
- <sup>15</sup>Hughes, D., J. Girkin, S. Poland, C. Longbottom, T. Button, J. Elgoyhen, H. Hughes, C. Meggs, and S. Cochran. Investigation of dental samples using a 35 MHz focussed ultrasound piezocomposite transducer. *Ultrasonics* 49:212–218, 2009.
- <sup>16</sup>Huysmans, M., and J. Thijssen. Ultrasonic measurement of enamel thickness: a tool for monitoring dental erosion? *J. Dent.* 28:187–191, 2000.
- <sup>17</sup>Irion, K., W. Nüssle, C. Löst, and U. Faust. Determination of the acoustical properties of enamel, dentin and alveolar bone. *Ultraschall in der Medizin (Stuttgart, Germany: 1980)* 7:87–93, 1986.
- <sup>18</sup>Jeffcoat, M., and M. Reddy. A comparison of probing and radiographic methods for detection of periodontal disease progression. *Curr. Opin. Dent.* 1:45–51, 1991.
- <sup>19</sup>Kao, R. T., and K. Pasquinelli. Thick vs. thin gingival tissue: a key determinant in tissue response to disease and restorative treatment. *J. Calif. Dent. Assoc.* 30:521–526, 2002.
- <sup>20</sup>Korostoff, J., A. Aratsu, B. Kasten, and M. Mupparapu. Radiologic assessment of the periodontal patient. *Dent. Clin. North Am.* 60:91–104, 2016.
- <sup>21</sup>Le, L. H. An investigation of pulse-timing techniques for broadband ultrasonic velocity determination in cancellous bone: a simulation study. *Phys. Med. Biol.* 43:2295, 1998.
- <sup>22</sup>Le, L. H., Y. J. Gu, Y. P. Li, and C. Zhang. Probing long bones with ultrasonic body waves. *Appl. Phys. Lett.* 96:114102, 2010.
- <sup>23</sup>Listgarten, M. Periodontal probing: what does it mean? *J. Clin. Periodontol.* 7:165–176, 1980.
- <sup>24</sup>Lopes, F. M., R. A. Markarian, C. L. Sendyk, C. P. Duarte, and V. E. Arana-Chavez. Swine teeth as potential substitutes for in vitro studies in tooth adhesion: a SEM observation. *Arch. Oral Biol.* 51:548–551, 2006.
- <sup>25</sup>Löst, C., K. M. Irion, and W. Nüssle. Determination of the facial/oral alveolar crest using RF-echograms. *J. Clin. Periodontol.* 16:539–544, 1989.
- <sup>26</sup>Ludlow, J. B., L. Davies-Ludlow, S. Brooks, and W. Howerton. Dosimetry of 3 CBCT devices for oral and maxillofacial radiology: CB Mercuray, NewTom 3G and i-CAT. *Dentomaxillofac. Radiol.* 35:219–226, 2014.
- <sup>27</sup>Misch, K. A., E. S. Yi, and D. P. Sarment. Accuracy of cone beam computed tomography for periodontal defect measurements. *J. Periodontol.* 77:1261–1266, 2006.
- <sup>28</sup>Mol, A. Imaging methods in periodontology. *Periodontol* 2000(34):34–48, 2004.
- <sup>29</sup>Nguyen, K.-C. T., L. H. Le, N. R. Kaipatur, and P. W. Major. Imaging the cemento-enamel junction using a 20-MHz ultrasonic transducer. *Ultrasound Med. Biol.* 42:333–338, 2016.
- <sup>30</sup>Nguyen, K. C. T., L. H. Le, T. N. H. T. Tran, M. D. Sacchi, and E. H. M. Lou. Excitation of ultrasonic Lamb waves using a phased array system with two array probes: phantom and in vitro bone studies. *Ultrasonics* 54:1178–1185, 2014.
- <sup>31</sup>Njeh, C., T. Fuerst, E. Diessel, and H. Genant. Is quantitative ultrasound dependent on bone structure? A reflection. *Osteoporos. Int.* 12:1–15, 2001.
- <sup>32</sup>Pihlstrom, B. L., B. S. Michalowicz, and N. W. Johnson. Periodontal diseases. *Lancet* 366:1809–1820, 2005.
- <sup>33</sup>Radu, C., B. M. Eugenia, H. Mihaela, S. Andrea, and B. A. Florin. Experimental model for measuring and characterisation of the dento-alveolar system using high frequencies ultrasound techniques. *Med. Ultrason.* 12:127–132, 2010.
- <sup>34</sup>Salmon, B., and D. Le Denmat. Intraoral ultrasonography: development of a specific high-frequency probe and clinical pilot study. *Clin. Oral Investig.* 16:643–649, 2012.
- <sup>35</sup>Savitha, B., and K. Vandana. Comparative assesment of gingival thickness using transgingival probing and ultrasonographic method. *Indian. J. Dent. Res.* 16:135, 2005.
- <sup>36</sup>Scarfe, W. C., and A. G. Farman. What is cone-beam CT and how does it work? *Dent. Clin. North Am.* 52:707–730, 2008.
- <sup>37</sup>Scarfe, W. C., A. G. Farman, and P. Sukovic. Clinical applications of cone-beam computed tomography in dental practice. *J. Can. Dent. Assoc.* 72:75, 2006.
- <sup>38</sup>Slak, B., A. Daabous, W. Bednarz, E. Strumban, and R. G. Maev. Assessment of gingival thickness using an ultrasonic dental system prototype: a comparison to traditional methods. *Ann. Anat.* 199:98–103, 2015.
- <sup>39</sup>The-Canadian-Dental-Association. Dentist Questions and Answers. 2014. [http://www.cda-adc.ca/\\_files/about/news\\_events/health\\_month/PDFs/dentist\\_questions\\_answers.pdf](http://www.cda-adc.ca/_files/about/news_events/health_month/PDFs/dentist_questions_answers.pdf). Accessed October 15, 2015.
- <sup>40</sup>Theodorakou, C., A. Walker, K. Horner, R. Pauwels, R. Bogaerts, R. Jacobs, and SEDENTEXCT Project Consortium. Estimation of paediatric organ and effective doses from dental cone beam CT using anthropomorphic phantoms. *Br. J. Radiol.* 85(1010):153–160, 2014.
- <sup>41</sup>Toda, S., T. Fujita, H. Arakawa, and K. Toda. An ultrasonic nondestructive technique for evaluating layer thickness in human teeth. *Sens. Actuators A Phys.* 125:1–9, 2005.
- <sup>42</sup>Tole, N. M., and H. Ostensen. Basic Physics of Ultrasonographic Imaging. Geneva: World Health Organization, 2005.
- <sup>43</sup>Tsoliis, F. I., I. G. Needleman, and G. S. Griffiths. Periodontal ultrasonography. *J. Clin. Periodontol.* 30:849–854, 2003.
- <sup>44</sup>Tyndall, D. A., and S. Rathore. Cone-beam CT diagnostic applications: caries, periodontal bone assessment, and endodontic applications. *Dent. Clin. North Am.* 52:825–841, 2008.
- <sup>45</sup>Vasconcelos, K. D., K. M. Evangelista, C. D. Rodrigues, C. Estrela, T. O. de Sousa, and M. A. G. Silva. Detection of periodontal bone loss using cone beam CT and intraoral radiography. *Dentomaxillofac. Rad.* 41:64–69, 2012.
- <sup>46</sup>Vayron, R., V. Mathieu, A. Michel, and G. Haïat. Assessment of in vitro dental implant primary stability using an ultrasonic method. *Ultrasound Med. Biol.* 40:2885–2894, 2014.
- <sup>47</sup>Vayron, R., E. Soffer, F. Anagnostou, and G. Haïat. Ultrasonic evaluation of dental implant osseointegration. *J. Biomech.* 47:3562–3568, 2014.
- <sup>48</sup>Walter, C., P. D. M. Dent, J. C. Schmidt, and K. Dula. Cone beam computed tomography (CBCT) for diagnosis and treatment planning in periodontology: a systematic



- review. *Quintessence Int. (Berlin, Germany: 1985)* 47:25–37, 2015.
- <sup>49</sup>Wang, S., Y. Liu, D. Fang, and S. Shi. The miniature pig: a useful large animal model for dental and orofacial research. *Oral Dis.* 13:530–537, 2007.
- <sup>50</sup>Xiang, X., M. G. Sowa, A. M. Iacopino, R. G. Maev, M. D. Hewko, A. Man, and K.-Z. Liu. An update on novel non-invasive approaches for periodontal diagnosis. *J. Periodontol.* 81:186–198, 2010.
- <sup>51</sup>Yoshida, H., H. Akizuki, and K.-I. Michi. Intraoral ultrasonic scanning as a diagnostic aid. *J. Craniomaxillofac. Surg.* 15:306–311, 1987.
- <sup>52</sup>Zimbran, A., S. Dudea, and D. Dudea. Evaluation of periodontal tissues using 40 MHz ultrasonography preliminary report. *Med. Ultrason.* 15:6–9, 2013.